Nanoscale

PAPER

View Article Online
View Journal | View Issue

Cite this: *Nanoscale*, 2023, **15**, 4940

Homogeneous in-plane WSe_2 P–N junctions for advanced optoelectronic devices†

Dewu Yue,[a] Xin Ju,*[b] Tao Hu,[a] Ximing Rong,[c] Xinke Liu,[c] Xiao Liu,[c] Hong Kuan Ng,[b] Dongzhi Chi,[b] Xinzhong Wang*[a] and Jing Wu*[b,d]

Received 9th November 2022,
Accepted 25th January 2023

DOI: 10.1039/d2nr06263a

rsc.li/nanoscale

Conventional doping schemes of silicon (Si) microelectronics are incompatible with atomically thick two-dimensional (2D) transition metal dichalcogenides (TMDCs), which makes it challenging to construct high-quality 2D homogeneous p–n junctions. Herein, we adopt a simple yet effective plasma-treated doping method to seamlessly construct a lateral 2D WSe_2 p–n homojunction. WSe_2 with ambipolar transport properties was exposed to O_2 plasma to form WO_x on the surface in a self-limiting process that induces hole doping in the underlying WSe_2 *via* electron transfer. Different electrical behaviors were observed between the as-exfoliated (ambipolar) region and the O_2 plasma-treated (p-doped) region under electrostatic modulation of the back-gate bias (V_{BG}), which produces a p–n in-plane homojunction. More importantly, a small contact resistance of 710 Ω μm with a p-doped region transistor mobility of ~157 $cm^2\ V^{-1}\ s^{-1}$ was achieved due to the transformation of Schottky contact into Ohmic contact after plasma treatment. This effectively avoids Fermi-level pinning and significantly improves the performance of photodetectors. The resultant WSe_2 p–n junction device thus exhibits a high photoresponsivity of ~7.1 × 10^4 mA W^{-1} and a superior external quantum efficiency of ~228%. Also, the physical mechanism of charge transfer in the WSe_2 p–n homojunction was analyzed. Our proposed strategy offers a powerful route to realize low contact resistance and high photoresponsivity in 2D TMDC-based optoelectronic devices, paving the way for next-generation atomic-thickness optoelectronics.

1. Introduction

Two-dimensional (2D) materials, such as transition metal dichalcogenides (TMDCs), hold promise as fundamental building blocks for next-generation flexible electronic and optoelectronic devices because of their tunable bandgap, high mobility, good chemical stability, and ability to form high-quality interfaces in van der Waals (vdW) heterostructures.[1–5] Among all TMDCs, WSe_2 is an intriguing 2D material that offers bipolar transport characteristics with thickness-dependent band gaps of 1.7 eV (direct, monolayer) and approximately 1.2 eV (indirect, multilayer), as well as theoretical electron and hole motilities of about 250 and 270 $cm^2\ V^{-1}\ s^{-1}$, respectively.[6–8] Owing to its unique physical properties, WSe_2 has opened the door to versatile electronic and optoelectronic devices with excellent optoelectronic performance. In recent years, new artificial structures based on van der Waals (vdW) vertical heterostructures or lateral p–n heterojunctions have attracted great interest in the application of WSe_2 optoelectronic devices.[9–14] For instance, Jo and co-workers demonstrated that the photoresponsivity of WSe_2/h-BN-based p–n heterojunction photodetectors was remarkably improved by a triphenylphoshine n-doping method.[15] Guo and co-workers reported that a WSe_2–ZnO p–n heterojunction photodetector fabricated by combining p-type WSe_2 and n-type ZnO exhibited an ultra-high photoresponsivity of 4.83 × 10^3 A W^{-1} under 405 nm light illumination.[16] Liu *et al.* reported that a photodetector based on a WSe_2–Bi_2Te_3 p–n heterojunction can give rise to a fast response time of ~210 μs and a high photoresponsivity of ~20.5 A W^{-1} under 633 nm illumination.[17] These results have demonstrated that the successful construction of heterojunctions can significantly improve the photoresponse characteristics of TMDC-based devices, which, however, still suffer from unavoidable residues and complex flake alignment processes, *i.e.*, difficult to localize the target

[a]*Information Technology Research Institute, Shenzhen Institute of Information Technology, Shenzhen, 518172, China. E-mail: wangxz@sziit.com.cn*
[b]*Institute of Materials Research and Engineering (IMRE), Agency for Science, Technology and Research (A*STAR), 2 Fusionopolis Way, Innovis #08-03, Singapore 138634, Singapore. E-mail: ju_xin@imre.a-star.edu.sg, wujing@imre.a-star.edu.sg*
[c]*College of Materials Science and Engineering, Shenzhen Key Laboratory of Special Functional Materials, Shenzhen Engineering Laboratory for Advanced Technology of Ceramics, Guangdong Research Center for Interfacial Engineering of Functional Materials, Shenzhen University, Shenzhen 518060, China*
[d]*Department of Materials Science and Engineering, National University of Singapore, 9 Engineering Drive 1, Singapore 117575, Singapore*
† Electronic supplementary information (ESI) available. See DOI: https://doi.org/10.1039/d2nr06263a

material onto another flake accurately.[18] In addition, the presence of a vdW gap between junctions may inhibit carrier charge transfer, which is generally undesirable for the device performance. As an alternative strategy, homogeneous junctions offer intrinsic advantages over heterogeneous junctions by providing clean and self-aligned interfaces.

Since the Fermi level (E_F) of WSe_2 resides in the middle of the band gap, its ambipolar nature allows for electron or hole dominant transport *via* selective doping, which can be used as an ideal candidate for the implementation of p–n photodiodes, photovoltaic cells, and complementary logic systems.[19–23] However, the *in situ* synthesis of high-quality homogeneous WSe_2 p–n junction-based photodetectors still faces many hurdles, such as the complex fabrication process, slow photoresponsivity, low photodetectivity, *etc*. On the other hand, the formation of a Schottky barrier (SB) at the WSe_2–metal interface inevitably results in a high contact resistance (R_c).[24,25] Furthermore, the physical metal deposition process may cause potential lattice disorders or even local destruction of the material, leading to Fermi-level pinning or poor band alignment, ultimately limiting the efficiency of photodiodes.[26–28] Consequently, carrier transport can only be carried out by tunneling through thin SBs, resulting in a low current density. To overcome the inherent performance limits of 2D TMDCs and to improve the contact problems on WSe_2 functional devices, various doping schemes, work function engineering techniques, electrical tuning techniques, *etc.* have been explored.[29–35] However, these methods are relatively complicated and require high temperature or vacuum process conditions, which greatly hinder their practical application in constructing high-performance WSe_2-based photodetectors. Most recently, transition metal oxides (TMOs) used in organic electronics and 2D material-based electronic devices have been demonstrated as effective p-type contacts and dopants.[36,37] This doping scheme has been widely developed and applied in complementary metal–oxide–semiconductor (CMOS) technology. Despite many encouraging outcomes so far, the fabrication of a 2D TMDC p–n homojunction with low R_c is still limited by technical challenges.

In this work, we demonstrate an efficient and reliable approach by performing O_2 plasma treatment to easily permit the amplification of hole transport, and thus achieve *in situ* p-type semiconductor characteristics in WSe_2. The under-stoichiometric oxidation of WSe_2 into WO_x highly induces hole doping in the neighboring (or underlying) WSe_2 *via* electron transfer from the underlying WSe_2 to the top oxidized WO_x layer. Moreover, our results revealed that the transformation of the SB to Ohmic contact arising from plasma treatment greatly increases the hole mobility from ~22 to ~157 $cm^2\ V^{-1}\ s^{-1}$ in a p-type doped WSe_2 transistor. As a result, the as-fabricated in-plane p–n homojunction exhibits a superior external quantum efficiency of ~228%, an excellent photoresponsivity of ~7.1×10^4 $mA\ W^{-1}$, and a photodetectivity of ~3×10^3 Jones under 532 nm light illumination. The resultant device performance of our method proves it to be an ideal strategy for constructing high-performance p–n junction optoelectronic devices by using self-oxidizing 2D TMDCs, which may be applied to other TMDCs for future multifunctional electronic and optoelectronic applications.

2. Results and discussion

Fig. 1(a) shows the schematic illustration of a pristine and plasma-treated WSe_2. The WSe_2 flake was treated with physical O_2 plasma bombardment where the Se atoms were replaced by O atoms, which then forms a WO_x layer on the surface of the WSe_2 flake. The same sample was repeatedly subjected to plasma treatment, and the transfer characteristics of the as-fabricated WSe_2 FET at cumulative plasma durations of 5 to 120 s were measured (Fig. S1†). A change in the majority of carriers, from electrons to holes (n-dominant ambipolar to strong p-type), is observed with an on/off ratio reaching 10^8 after 120 s of O_2 plasma treatment as shown in Fig. S1.† As a result, the topmost layers of the WSe_2 flake were completely oxidized into WO_x, consistent with previous reports where WO_x is used as an effective doping layer.[23] In addition, the thickness of the WSe_2 flakes increased by ~1 nm after O_2 plasma treatment (Fig. 1(b)), which is an indication of the formation of a thin layer of WO_x atop the WSe_2 flake. The oxidation depth of the WSe_2 flake was subsequently assessed using the secondary-ion mass spectrometry (SIMS) technique. As shown in Fig. S2,† oxidation is found to be a self-limiting process. The depth of the oxide layer (WO_x, including WO^-, WO_2^-, and WO_3^-) is determined to be approximately 1.2 nm, which is restricted only in the very top layer, therefore offering an easy and efficient control of the oxide thickness. To further validate the formation of the WO_x layer, the surface composition of the plasma-treated WSe_2 was further analyzed using X-ray photoelectron spectroscopy (XPS), as presented in Fig. 1(c). The XPS core spectrum of the pristine WSe_2 shows

Jing Wu

Dr Jing Wu received his bachelor's degree in Physics from Zhejiang University in 2010 and his PhD in physics from the National University of Singapore (NUS) in 2015. He is currently the group leader of the Nano Electronic and Thermal Transport (NETT) group at the Institute of Materials Research and Engineering (IMRE) and an adjunct faculty member in the Department of Materials Science and Engineering, NUS. His research interests focus on the exotic transport dynamics and scattering physics of 2D materials, such as charge transport, thermoelectric and optoelectronic transport, and exploring the technical aspects for high-performance electronics.

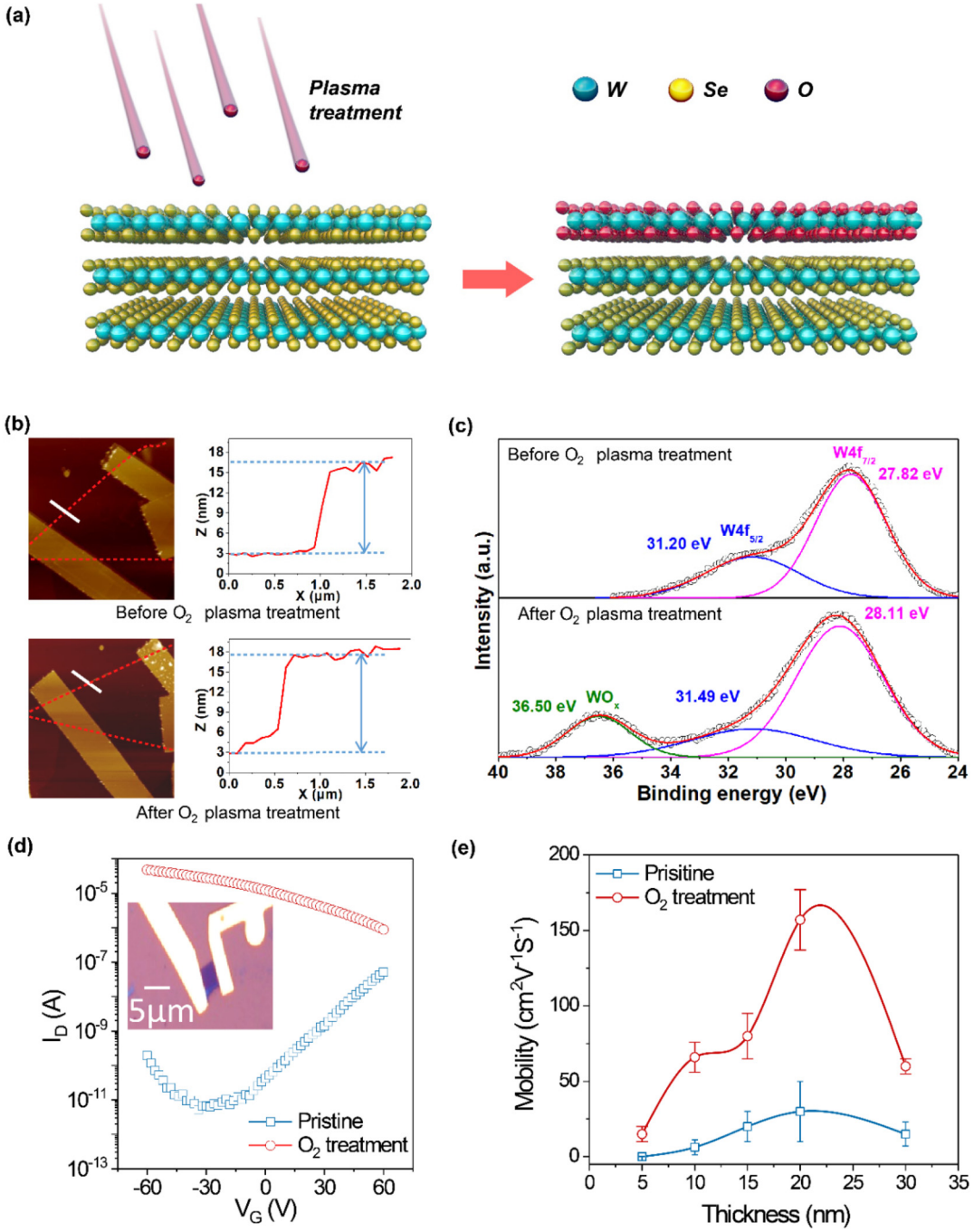

Fig. 1 (a) Schematic illustration of O_2 plasma treatment of bulk WSe_2. (b) The AFM images of a WSe_2 flake before and after O_2 plasma treatment, and the right part shows the AFM height profile revealing the thickness of the ~13 nm WSe_2 flake. (c) The XPS spectral comparison shows the existence of one extra peak at a binding energy of 36.50 eV corresponding to WO_x and a slight shift in the binding energies of W peaks after O_2 plasma treatment. (d) Transfer characteristics of a WSe_2 FET with V_d = 1 V before and after O_2 plasma treatment. The inset shows the optical image of the as-fabricated WSe_2 FET. (e) The mobility obtained from WSe_2 FETs of different thicknesses.

two main peaks at 27.82 and 31.20 eV corresponding to W $4f_{7/2}$ and W $4f_{5/2}$, respectively.[38,39] In comparison, the W $4f_{7/2}$ (28.11 eV) and W $4f_{5/2}$ (31.49 eV) peaks of the plasma-treated WSe_2 showed a slight shift to higher binding energies. Moreover, a clear additional peak can be observed at the binding energy of 36.50 eV corresponding to WO_x ($x \leq 3$),[40] which verifies the presence of WO_x at the top of WSe_2 flakes. These results demonstrate that oxygen radicals are efficiently doped into WSe_2 crystals during plasma exposure. Furthermore, the transport characteristics of the pristine and plasma-treated WSe_2-based FETs were investigated under an applied gate voltage from −60 to 60 V. The optical microphotograph of the plasma treated WSe_2 based-FET is presented in the inset of Fig. 1(d). The pristine WSe_2-based FET exhibits n-type dominated ambi-

polar characteristics, as shown in Fig. 1(d). However, after O_2 plasma treatment, the transfer curve shows a heavily p-doped characteristic (Fig. 1(d)). These results confirm the modulation of the as-fabricated WSe_2 channels with O_2 plasma, which act as p-type dopants when exposed to controlled plasma conditions.[41] The field-effect mobility (μ_{FE}) can be calculated from the following formula $\mu_{FE} = g_m L_c h/C_{ox} W_{ch} V_{SD}$,[42] where L_{ch} and W_{ch} are the channel length and width, respectively, $C_{ox} = 1.15 \times 10^{-8}$ F cm^{-2} for 300 nm SiO_2, $g_m = \partial I_D/\partial V_{BG}$ is the transconductance, and V_{SD} is the source–drain voltage. The maximum μ_{FE} of the as-fabricated WSe_2 FETs is found to be about 157 cm^2 V^{-1} s^{-1}, which is much higher than previously reported results (see Table 1). Fig. 1(e) shows the μ_{FE} of the pristine and O_2-treated WSe_2 devices fabricated with different thicknesses from 5 nm to 30 nm, where the FET mobility is significantly increased by up to a factor of 8 after O_2 plasma-induced p-type doping. We believe that the high mobility obtained may be attributed to the lowering of the contact resistance (R_c) by plasma doping.

It is well-known that a high contact resistance R_c would significantly affect the electrical and optical performances of TMDC-based FETs.[30] Hence, we fabricated devices with the same channel width and different channel lengths ranging from 2 to 5 μm to evaluate the contact R_c of the p-doped WSe_2 channels by the transmission line method (TLM). Fig. 2(a) shows the optical images of the WSe_2 devices with varied channel lengths for examining contact properties. The enlarged schematic in Fig. 2(a) illustrates the carrier pathways (yellow arrows) in the channel of the plasma-treated device, where the electron transfer from the underlying WSe_2 to the surface WO_x contributes to the formation of electron transport paths (red arrows) from the channel to the doping layer, which is consistent with previous reports.[23,43,44] In particular, a thin WO_x layer formed after the oxygen plasma treatment will attract electrons from the neighboring (or underlying) WSe_2, thereby inducing the heavily p-doped WSe_2, *i.e.*, the formation of a conducting channel of holes. The transfer characteristics of these devices are shown in Fig. S3.† Fig. 2(b) and (c) show the output characteristics obtained from the pristine and O_2 plasma-treated WSe_2-based FETs, respectively. The non-linear increase of hole current with increasing drain bias (V_D) indicates a large SB between the metal and pristine WSe_2 layers (see Fig. 2(b)). In contrast, the excellent linear characteristics of the output curve of the O_2-plasma treated WSe_2 layers in Fig. 2(c) suggest the conversion of Schottky contact into Ohmic-like behavior. This may be attributed to the shift of the Fermi level towards the valence band maximum (VBM) of WSe_2: p-type dominant conversion. We believe that this phenomenon contributes to the transition from Schottky emission to direct tunneling for easier hole injection. For Schottky emission,[45] $I = I_{SE} \exp(A\sqrt{V})$, where I_{SE} and A (>0) are two parameters related to Schottky emission behavior. For F–N tunneling or FNT,[46] $I = I_{FN} V^2 \exp(B/V)$, where I_{FN} and B (<0) are two parameters related to F–N tunneling behavior. To better elucidate the transition from Schottky emission to direct tunneling, the I–V curves are plotted in the forms of ln I-*vs.*-$V^{1/2}$ and ln(I/V^2)-*vs.*-V^{-1}, respectively. Fig. S4† shows that before plasma treatment, the channel is dominated by Schottky emission, while after plasma treatment, the F–N tunneling becomes dominant. To further quantify the variation in R_c after plasma treatment, Fig. 2(d) shows the linear fitting of the total resistance (R_{total}) as a function of channel length (L). R_{total} could be described as $R_{total} = LR_{ch}/W + 2R_c$,[47] where R_c is the contact resistance, W is the channel width, L is the channel length, and R_{ch} is the 2D channel resistance. The value of R_c can be directly extracted from the y-intercept of the linear fit to R_{total}. Fig. 2(e) shows R_c ranging from 0.71 to 6.73 kΩ μm under different gate voltages ranging from −60 to 60 V. Considering the small thickness of the channel, uniform doping leads to a uniform current distribution in the vertical direction. A high gate bias leads to an increase in carrier density and the narrowing of the potential barrier along the metal and the material interface. The elevated hole concentration and narrowed potential barrier aid in the injection of carriers into the WSe_2 channel and thereby achieve a transition from Schottky emission to direct tunneling. As a result, a lower contact resistance is obtained.[47] In particular, the lowest R_c of ∼710 Ω μm measured at $V_{BG} = -60$ V can be successfully achieved in the plasma-treated WSe_2 FETs, suggesting a reduction in R_c after the plasma treatment. It should be noted that such a small R_c highlights the importance of the self-terminating oxidation process, resulting in the thinnest oxide and therefore a transparent tunnel barrier for increased hole injection between the metal and WSe_2 as a key factor for the excellent device performance.

The p–n junction is crucial for the separation of photon-induced electron–hole (e–h) pairs towards achieving photodetectors with high responsivity or solar cells with high quantum efficiency.[48,49] Through oxidation doping, the partial doping of a WSe_2 FET results in a lateral p–n homojunction. To determine their optoelectronic performance, WSe_2 lateral junctions were fabricated. More detailed information regarding the device preparation process can be found in the Experimental section. Fig. 3(a) shows the schematic diagram and the optical image (top-view) of the fabricated WSe_2 devices. These WSe_2 devices were then exposed to O_2 plasma

Table 1 Comparison of the field-effect mobility with other WSe_2-based electronic devices

Materials	Field-effect mobility (cm^2 V^{-1} s^{-1})	Ref.
WSe_2 pn-junction	**157**	**This work**
WSe_2/MoS_2 heterojunction	8.42	6
$WSe_{2(1-x)}Te_{2x}$	46	7
WSe_2/ReS_2 pn-junction	16.5	10
WSe_2 pn-junction	36.28	11
Monolayer WSe_2	132	13
WSe_2/h-BN heterojunction	25.6	15
WO_x/WSe_2 heterojunction	40	23
WSe_2 flake	2.2	24
WSe_2/Graphene heterojunction	84	25
Monolayer WSe_2	82	28
WSe_2 flake	150	35

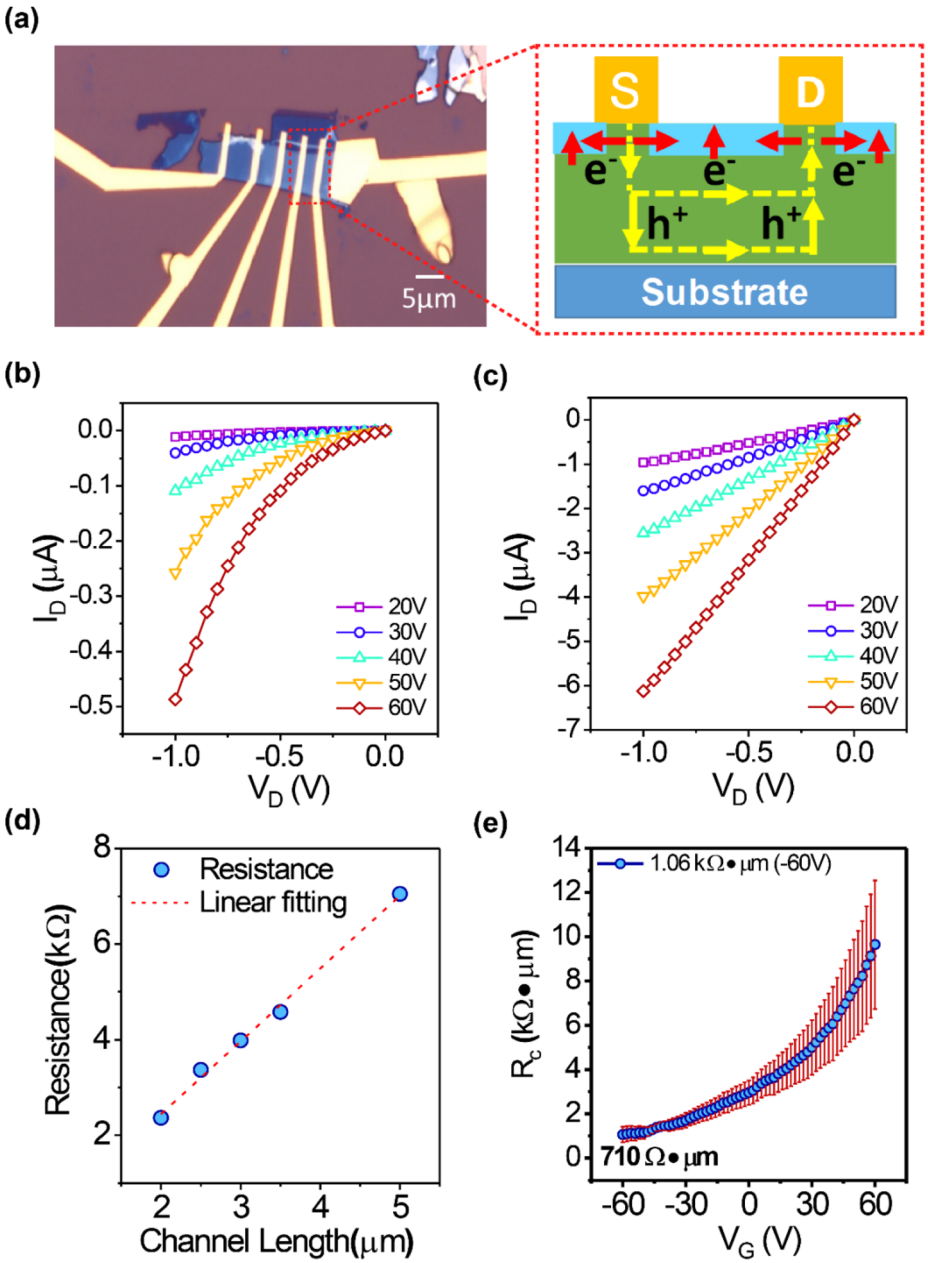

Fig. 2 Contact properties of the WSe_2 FETs obtained by TLM measurement. (a) Optical micrograph of the TLM devices. The enlarged section on the right side shows the hole transport path occurring in the whole channel, which can lead to low contact resistance and thus higher mobility. (b) Schottky contact can be clarified from the output characteristics of the pristine WSe_2 FETs. (c) By applying O_2 plasma treatment, Ohmic contact was achieved in WSe_2 FETs. (d) R_{total} as a function of channel length to extract R_c using a TLM linear fitting curve. (e) R_c *versus* bottom gate voltage in which the lowest R_c obtained was ~710 Ω μm at a V_{BG} of −60 V.

under different operating conditions (see the Experimental section). Note that a PMMA layer is employed as a mask to protect areas with electrodes 1 to 2, leaving areas with electrodes marked with 3 to 4 exposed for O_2 plasma treatment. The O_2 molecule was then chemisorbed onto the top surface of the exposed WSe_2, in which the top layer of the Se atom was substituted by an oxygen atom. Finally, the WO_x layer was formed on top of the WSe_2 layer. As a result of p-doping due to O_2 plasma (formation of a WO_x layer on the top of WSe_2), a p-type (n-type) dominant conduction is observed in the O_2 plasma-treated (plasma-protected) region. The typical transfer curves of the pristine WSe_2 channel (through electrodes 1 to 2) were measured to maintain n-type behaviour (Fig. 3(b)). The electrical performance of the as-prepared plasma-treated channel was then measured through electrodes 3 to 4 (Fig. 3(c) and Fig. S5†), yielding p-type characteristics. With the capability of achieving both unipolar p-type (plasma-treated) and n-type (pristine) conduction behaviours, a lateral p–n homojunction

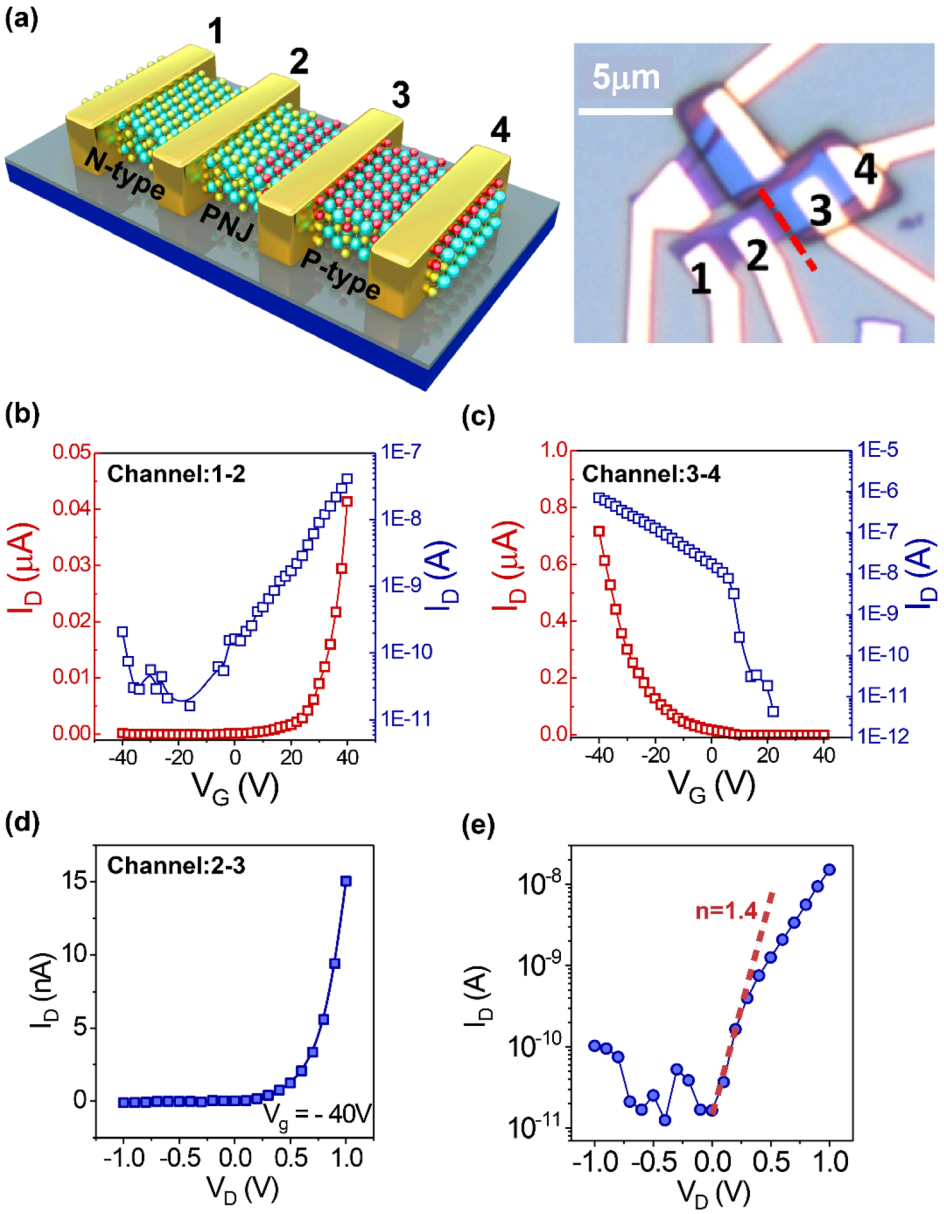

Fig. 3 (a) 3D schematic structure and optical photograph (right side) of an O_2 plasma-treated WSe_2 FET device showing channels 1–2, 2–3, and 3–4 as n-WSe_2, pn-WSe_2, and p-WSe_2, respectively. (b) and (c) The transfer curves of n- and p-WSe_2 channels measured at V_d = 1 V after O_2 plasma treatment, which are represented in both linear and logarithmic scales. (d) The output curve of an O_2 plasma-treated WSe_2 p–n junction device obtained at V_g = −40 V is represented on a linear scale. (e) The output curve is represented on a logarithmic scale to calculate the p–n junction ideality factor as 1.4.

can then be fabricated using a single WSe_2 flake. Fig. 3(d) and (e) show the corresponding $I_d - V_d$ output curves of the partially doped WSe_2 device (channel: electrodes 2–3) with V_g = −40 V in the linear (left) and log (right) scales, in which little to no current flow is observed under reverse source–drain bias (V_d < 0 V). However, a much higher current flow can be observed when a forward bias is applied (V_d > 0 V), indicating the forward rectifying diode behavior. Furthermore, an ideality factor (n)[50,51] of 1.4 was calculated from the dark current (Fig. 3(e)), indicating the formation of a near-ideal p–n junction.[52,53] It is known that n = 1 indicates an ideal p–n junction diode, n ranging between 1 and 2 implies the existence of a tunneling current, and n = 2 indicates the existence of defects or interface traps that drives the recombination process.[54] Thus, our good ideality factor of ~1.4 can be ascribed to the low charge trap density at the homojunction interface.[55] The above results prove the successful preparation of a p–n junction between electrodes 2 and 3. However, it should be noted that the p–n WSe_2 device is formed with a Schottky junction in the n-type part of WSe_2 (contact 2), p–n junctions in the channel (electrodes 2–3), and Ohmic-like contact in the p-type part of WSe_2 (contact 3).

Next, we explored the optoelectronic properties of p–n WSe_2 homojunction photodetectors. The transfer curves of the as-fabricated photodetector were measured in the dark and 532 nm illumination. By comparison, a photocurrent response characteristic under light irradiation is observed in Fig. 4(a), which may be mainly attributed to the strong light absorption in the WSe_2 p–n junction. This then generates a larger density of photoinduced e–h pairs which leads to a reduction of the Schottky barrier, thereby allowing the photogenerated carriers to transmit more effectively along the metal/WSe_2 interface under an externally applied bias. To further investigate the performance of WSe_2 p–n junction photodetectors and to study their dynamic optical response, time (T)- and gate voltage (V_G)-dependent photocurrent measurements under a fixed source–drain bias of 1 V were performed as shown in Fig. 4(b). Here, the time (T)- and source–drain voltage (V_D)-dependent photocurrent of the WSe_2 p–n junction photodetectors was also measured at the fixed gate bias of 40 V (Fig. 4(c)). As V_G swept from +40 to −40 V, the photocurrent enhancement was observed under various V_D and V_G conditions. In particular, the maximum photocurrent is obtained under a gate bias voltage of 40 V. Meanwhile, prominent variations in the gate-dependent photocurrent can be obtained at both $V_G < 0$ V and $V_G > 0$ V sides. These results suggest that the photocurrent response can be effectively modulated by the gate electric field. In addition, the photocurrent is observed to slightly decrease with time under continuous light irradiation, indicating possible charge trapping effects. Higher gate voltage (40 V) leads to an increase in carrier concentration while the potential barrier at the contact interface becomes narrower. Thus, the charge trap states are relatively more easily filled with carriers, leading to a slight reduction in photocurrent. In contrast, at a gate voltage of 0 V, when the Fermi level is in equilibrium, the carrier density is relatively low. As such, carriers are difficult to be captured by trap states, so minimal photocurrent changes are observed in time-dependent photocurrent measurements (Fig. S6†). The photocurrent characteristics of the junction can be further understood through the energy band diagrams, as shown in Fig. 4(d)–(f). Fig. 4(d) shows the band diagram of the WSe_2 p–n junction in the equilibrium state. The Fermi level of the p-type area is near to the valence band, whereas the Fermi level of the n-type part is near to the conduction band. Under reverse bias, the energy barrier at the junction becomes higher as the width of the depletion region increases. Consequently, electrons cannot transmit effectively, and the p–n junction is in the OFF state. Under forward bias, the energy barrier becomes lower, thus allowing electrons to easily pass through the junction, and the p–n junction is in the ON state. This typical p–n junction behavior is consistent with the output curve as shown in Fig. 3(d). Furthermore, the mechanism of photocurrent generated in the dark (Fig. 4(e)) and light (Fig. 4(f)) states was also proposed. When the negative gate voltage is applied in the dark state (Fig. 4(e)), the Fermi level drops below the valence band of the p-type branch, which enables holes to flow easily from the junction into the metal. As a result, there is no current in the p–n junction. When a positive gate voltage is applied, the Fermi level moves into the conduction band in the n-type branch, which allows electrons to easily transfer from the junction into the metal. Therefore, the designed lateral p–n junction shows no current when electrons are dominant carriers. Under light irradiation, the generation of e–h pairs takes place near the depletion region, and the photoexcited carriers are swept from the junction in opposite directions by an externally applied bias, resulting in a net increase in photocurrent, as shown in Fig. 4(f). As a result, internal hole and electron transport combined with the resulting overdose e–h pairs from light absorption increases the current, which is much higher than the dark state (as shown in Fig. 4(e)) even at low gate voltages. In both positive and negative gate biases, the photocurrent is high as the substantial photogenerated e–h pairs can be readily separated and driven toward the cathode and anode contacts in the *in situ* WSe_2 lateral p–n junction.

Next, we further investigated the photoresponse of the designed WSe_2 p–n junction by measuring the I_D–V_D characteristics at the gate bias of −40 V and 40 V, respectively. Under different powers of light illumination (6, 16, 31, and 42 mW), the WSe_2 p–n junction exhibited ideal diode characteristics as shown in Fig. 4(g) and (h). The photoresponse figures of merit such as photoresponsivity (R), external quantum efficiency (EQE), and detectivity (D^*) are sequentially evaluated. The spectral responses of WSe_2 photodetectors were expressed through R, which is defined as the ratio of the photocurrent and the incident laser power, *i.e.*, $R = I_{ph}/P_{Laser}$, where I_{ph} is the photocurrent = $|I_{light} - I_{dark}|$, and P_{Laser} is the incident laser power per unit area. Here, $I_{ph} = |I_{light} - I_{dark}| = 6 \times 10^{-6}$ A, $P = L{\cdot}W/(\pi{\cdot}r^2){\cdot}P_m = 3.5 \times 2.5/(3.14 \times 30^2) \times 2.7 \times 10^{-5} = 8.4 \times 10^{-8}$ W, in which L and W are the channel length and channel width, r is the radius, and P_m is the power measured by a power meter. Fig. 4(i) shows the photoresponsivities of the WSe_2 photodetector as a function of incident laser power. Another crucial figure of merit for the photodetector is the EQE, which is given by EQE (%) = $100{\cdot}hcR/e\lambda$, where h is Planck's constant (6.63×10^{-34} j s), c is the speed of light (3×10^8 m s^{-1}), e is the unit charge, and λ is the wavelength of incident light (λ = 532 nm). The EQE of a photodetector represents the ratio of the total number of charge carriers generated to the number of incident photons. Through the above equations, the R and EQE of our p–n junction are calculated to be ~7.1×10^4 mA W^{-1} and ~228%, respectively, outperforming other reported results as summarized in Table 2.[10,12,14–17,19,56–59] The high values of R and EQE also demonstrate that the plasma-treated WSe_2 p–n junction exhibits a good photoresponsivity. In addition, D^* is another figure of merit for photodetector devices to evaluate the detector sensitivity, which is generally calculated using the following equation of D^* (Jones) = $(R{\cdot}A^{1/2})/(I_{dark}{\cdot}2e)^{1/2}$. The D^* value obtained for our designed WSe_2 p–n junction photodetector was about 3×10^3 Jones. These results prove the effectiveness of O_2 plasma treatment for achieving high-performance WSe_2-based optoelectronic devices.

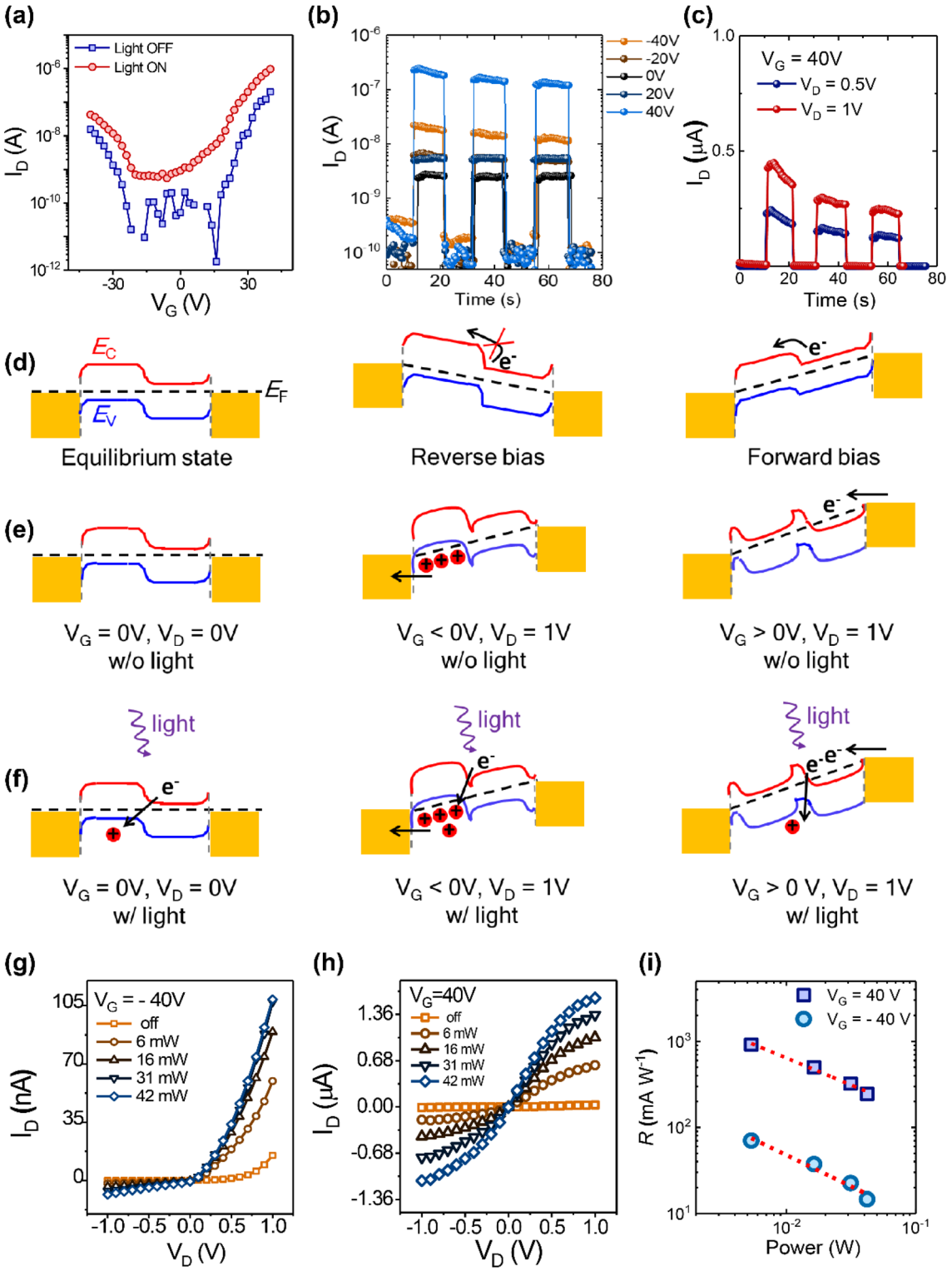

Fig. 4 (a) Typical photoresponse of the WSe_2 p–n homojunction FET devices under 532 nm illumination at different gate biases demonstrating clear photovoltaic behavior. (b) and (c) Time-dependent photocurrent measurements of pn-WSe_2 achieved under 532 nm laser irradiation at the applied V_d = 1 V with various V_g values and fixed V_g = 40 V with various V_d values. (d–f) The corresponding energy band diagrams show the carrier transport paths in the WSe_2 p–n homojunction device with and without light irradiation at the applied gate bias. (g) and (h) The photocurrents of the as-fabricated WSe_2 p–n homojunction under different powers of light illumination (5.35, 16, 31 and 42 mW) at gate biases of −40 V and 40 V, respectively. (i) The photoresponsivity (R) of the WSe_2 p–n junction obtained under gate biases of −40 V and 40 V as a function of light power. The responsivity was linear with the incident optical power.

Table 2 Comparison of R with other WSe_2-based devices

Materials	Light irradiation conditions (nm)	R (mA W^{-1})	Response time (ms)	Ref.
WSe_2 pn-junction	**532**	**7.1×10^4**	**42**	**This work**
WSe_2/ReS_2 pn-junction	532	3×10^3	0.004	10
WSe_2 pn-junction	520	80	0.106	12
$WSe_2/MoSe_2$ heterojunction	1550	127		14
WSe_2/h-BN junction	520	1.27×10^9	38.2–97	15
WSe_2/ZnO junction	405	4.83×10^6	0.01	16
WSe_2/Bi_2Te_3 pn-junction	633	2.05×10^4	0.21	17
p-Doped WSe_2	735	600	0.008	19
Multi-layer WSe_2	532	100	0.01	56
$WSe_2/BP/MoS_2$ heterojunction	532	6.32×10^3		57
Multi-layer WSe_2/pentacene	638	1.93×10^4		58
WSe_2/MoS_2 heterojunction	532	3.4		59

3. Conclusion

In summary, lateral p–n homojunctions were successfully fabricated from bulk WSe_2 *via* oxygen plasma doping and demonstrated in gate-modulated photodetector applications. After the plasma treatment, the lowest R_c of ~710 Ω μm of the WSe_2 p–n junction can be achieved, which is attributed to the highly p-doped WSe_2 that converts the Schottky barrier to Ohmic contact between the metal and WSe_2 interface. Thanks to the low R_c and excellent mobility of ~157 cm^2 V^{-1} s^{-1}, our plasma-treated WSe_2 p–n junction exhibited an exceptional photoresponsivity of ~7.1×10^4 mA W^{-1}, a superior external quantum efficiency of ~228%, and a detectivity of ~3×10^3 Jones under 532 nm light illumination wavelength. Our work provides an industry-compatible plasma doping technique to fabricate homogeneous in-plane p–n junctions for advanced 2-D optoelectronic device applications. Going forward, homogeneous complementary 2-D inverters can be fabricated by integrating the plasma-treated and as-exfoliated regions of a single WSe_2 layer to create basic building blocks for logic circuits. Our results contribute toward the realization of the local plasma treatment of WSe_2 flakes to tune the electrical properties of WSe_2 and the feasibility of fabricating WSe_2-based optoelectronic logic applications.

4. Experimental section

Fabrication of pristine WSe_2-based FETs and p-type WSe_2-based FETs

The synthesis process of the pristine WSe_2-based device is given as follows: at first, the WSe_2 film was exfoliated from the crystalline bulk material (HQ Graphene, the Netherlands) onto a 300 nm-thick SiO_2/Si substrate. Next, electrodes were patterned using electron beam lithography (EBL), and then deposited with Cr/Au (5 nm/70 nm) using an electron beam/thermal evaporator. To obtain p-type WSe_2-based FETs, the as-fabricated pristine WSe_2-based FETs were treated with O_2 plasma (20 W, 120 s). Our used XPS model is Thermo Fisher (Microlab350) with magnesium light.

Fabrication of the WSe_2 p–n junction

The fabrication process of the WSe_2 p–n junction is as follows: first, the pristine WSe_2 device was spin-coated with PMMA (Microchem, A4 495) at a speed of 3000 rpm (60 s). The device was then annealed at 150 °C for 2 min on a hot plate. Afterward, another layer PMMA (Microchem, A6 950) was spin-coated on the top of PMMA A4 with the same process. Furthermore, to obtain the p–n junction structure, we used EBL along with a developer (mixed DI water and IPA solution at a ratio of 1 : 3) to open a channel near the electrode, followed by rinsing with IPA and drying under the N_2 gas blowing. Finally, O_2 plasma treatment is employed to treat the as-fabricated device to obtain the WSe_2 p–n junction structure. The electrical transfer performances of the devices were tested in a vacuum probe station (Keithley 4200) at 0.1 Pa. The photocurrent response performance was measured using a light source of 532 nm.

Photocurrent measurement

Solid-state laser diodes were used as illumination sources. The incident power of the lasers (P_m) was measured with an optical power meter (Newport model 1918-C) and a thermopile sensor (919P-003-10). We measured the photoresponse characteristics with a monochromator light source. The device was placed on the sample holder, and a continuous wave laser beam generated from the solid-state laser diode and controller (Thorlabs LPSC-520-FC and CLD1010LP for 520 nm (visible) and Thorlabs LPSC-852-FC and CLD1010LPfor 852 nm (near IR)) was focused onto the device through a 40× objective lens (Olympus LUCPlanFLN, 40×, NA = 0.6).

Conflicts of interest

The authors declare no conflict of interest.

Acknowledgements

This work was supported by the National Natural Science Foundation of China (Grant No.12104319), the Shenzhen Science and technology planning project (JSGG20201102152403008), the

Double High-levels Plan (11400-2022-010201-02332) and the Science and Technology Project of Shenzhen City (JSGG20210802154213040). J. W. acknowledges the Advanced Manufacturing and Engineering Young Individual Research Grant (AME YIRG Grant No.: A2084c170) and the SERC Central Research Fund (CRF); J. W. and D. C. acknowledge the National Research Foundation Competitive Research Programme (NRFCRP24-2020-0002).

References

1 H. Xu, X. Han, X. Dai, W. Liu, J. Wu, J. Zhu, D. Kim, G. Zou, K. A. Sablon, A. Sergeev, Z. Guo and H. Liu, *Adv. Mater.*, 2018, **30**, 1706561.
2 P. Gant, P. Huang, D. Pérez de Lara, D. Guo, R. Frisenda and A. Castellanos-Gomez, *Mater. Today*, 2019, **27**, 8–13.
3 N. Flory, P. Ma, Y. Salamin, A. Emboras, T. Taniguchi, K. Watanabe, J. Leuthold and L. Novotny, *Nat. Nanotechnol.*, 2020, **15**, 118–124.
4 H. K. Ng, D. Xiang, A. Suwardi, G. Hu, K. Yang, Y. Zhao, T. Liu, Z. Cao, H. Liu, S. Li, J. Cao, Q. Zhu, Z. Dong, C. K. I. Tan, D. Chi, C.-W. Qiu, K. Hippalgaonkar, G. Eda, M. Yang and J. Wu, *Nat. Electron.*, 2022, **5**, 489–496.
5 T. Liu, D. Xiang, H. K. Ng, Z. Han, K. Hippalgaonkar, A. Suwardi, J. Martin, S. Garaj and J. Wu, *Adv. Sci.*, 2022, **9**(20), 2200816.
6 G. H. Shin, C. Park, K. J. Lee, H. J. Jin and S. Y. Choi, *Nano Lett.*, 2020, **20**(8), 5741–5748.
7 P. Yu, J. Lin, L. Sun, Q. L. Le, X. Yu, G. Gao, C. H. Hsu, D. Wu, T. R. Chang, Q. Zeng, F. Liu, Q. J. Wang, H. T. Jeng, H. Lin, A. Trampert, Z. Shen, K. Suenaga and Z. Liu, *Adv. Mater.*, 2017, **29**(4), 1603991.
8 S. Ahmed, X. Ding, P. P. Murmu, N. Bao, R. Liu, J. Kennedy, L. Wang, J. Ding, T. Wu, A. Vinu and J. Yi, *Small*, 2020, **16**, 1903173.
9 S. Jia, Z. Jin, J. Zhang, J. Yuan, W. Chen, W. Feng, P. Hu, P. M. Ajayan and J. Lou, *Small*, 2020, **16**, 2002263.
10 A. Varghese, D. Saha, K. Thakar, V. Jindal, S. Ghosh, N. V. Medhekar, S. Ghosh and S. Lodha, *Nano Lett.*, 2020, **20**(3), 1707–1717.
11 J. Sun, Y. Wang, S. Guo, B. Wan, L. Dong, Y. Gu, C. Song, C. Pan, Q. Zhang, L. Gu, F. Pan and J. Zhang, *Adv. Mater.*, 2020, **32**, 1906499.
12 Y. Tang, Z. Wang, P. Wang, F. Wu, Y. Wang, Y. Chen, H. Wang, M. Peng, C. Shan, Z. Zhu, S. Qin and W. Hu, *Small*, 2019, **15**, 1805545.
13 A. S. Bandyopadhyay, N. Adhikari and A. B. Kaul, *Chem. Mater.*, 2019, **31**(23), 9861–9874.
14 H. Xue, Y. Wang, Y. Dai, W. Kim, H. Jussila, M. Qi, J. Susoma, Z. Ren, Q. Dai, J. Zhao, K. Halonen, H. Lipsanen, X. Wang, X. Gan and Z. Sun, *Adv. Funct. Mater.*, 2018, **28**, 1804388.
15 S. H. Jo, D. H. Kang, J. Shim, J. Jeon, M. H. Jeon, G. Yoo, J. Kim, J. Lee, G. Y. Yeom, S. Lee, H. Y. Yu, C. Choi and J. H. Park, *Adv. Mater.*, 2016, **28**(24), 4824–4831.
16 N. Guo, L. Xiao, F. Gong, M. Luo, F. Wang, Y. Jia, H. Chang, J. Liu, Q. Li, Y. Wu, Y. Wang, C. Shan, Y. Xu, P. Zhou and W. Hu, *Adv. Sci.*, 2020, **7**, 1901637.
17 H. Liu, X. Zhu, X. Sun, C. Zhu, W. Huang, X. Zhang, B. Zheng, Z. Zou, Z. Luo, X. Wang, D. Li and A. Pan, *ACS Nano*, 2019, **13**(11), 13573–13580.
18 R. Cheng, D. Li, H. Zhou, C. Wang, A. Yin, S. Jiang, Y. Liu, Y. Chen, Y. Huang and X. Duan, *Nano Lett.*, 2014, **14**(10), 5590–5597.
19 T. Wang, K. Andrews, A. Bowman, T. Hong, M. Koehler, J. Yan, D. Mandrus, Z. Zhou and Y. Q. Xu, *Nano Lett.*, 2018, **18**(5), 2766–2771.
20 D. Li, M. Chen, Z. Sun, P. Yu, Z. Liu, P. M. Ajayan and Z. Zhang, *Nat. Nanotechnol.*, 2017, **12**, 901–906.
21 Y. Ren, X. Yang, L. Zhou, J. Y. Mao, S. T. Han and Y. Zhou, *Adv. Funct. Mater.*, 2019, **29**, 1902105.
22 M. V. Gustafsson, M. Yankowitz, C. Forsythe, D. Rhodes, K. Watanabe, T. Taniguchi, J. Hone, X. Zhu and C. R. Dean, *Nat. Mater.*, 2018, **17**, 411–415.
23 X. Liu, D. Qu, Y. Yuan, J. Sun and W. J. Yoo, *ACS Appl. Mater. Interfaces*, 2020, **12**(23), 26586–26592.
24 S. J. Yang, K. T. Park, J. Im, S. Hong, Y. Lee, B. W. Min, K. Kim and S. Im, *Nat. Commun.*, 2020, **11**, 1574.
25 H. L. Tang, M. H. Chiu, C. C. Tseng, S. H. Yang, K. J. Hou, S. Y. Wei, J. K. Huang, Y. F. Lin, C. H. Lien and L. J. Li, *ACS Nano*, 2017, **11**(12), 12817–12823.
26 S. Fan, S. J. Yun, W. J. Yu and Y. H. Lee, *Adv. Sci.*, 2020, **7**, 1902751.
27 S. W. LaGasse, P. Dhakras, K. Watanabe, T. Taniguchi and J. U. Lee, *Adv. Mater.*, 2019, **31**, 1901392.
28 G. Dastgeer, M. F. Khan, G. Nazir, A. M. Afzal, S. Aftab, B. A. Naqvi, J. Cha, K. A. Min, Y. Jamil, J. Jung, S. Hong and J. Eom, *ACS Appl. Mater. Interfaces*, 2018, **10**(15), 13150–13157.
29 H. G. Ji, P. Solis-Fernandez, D. Yoshimura, M. Maruyama, T. Endo, Y. Miyata, S. Okada and H. Ago, *Adv. Mater.*, 2019, **31**, 1903613.
30 M. Si, C. Jiang, W. Chung, Y. Du, M. A. Alam and P. D. Ye, *Nano Lett.*, 2018, **18**(6), 3682–3687.
31 G. Dastgeer, M. F. Khan, J. Cha, A. M. Afzal, K. H. Min, B. M. Ko, H. Liu, S. Hong and J. Eom, *ACS Appl. Mater. Interfaces*, 2019, **11**(11), 10959–10966.
32 R. Zhou, V. Ostwal and J. Appenzeller, *Nano Lett.*, 2017, **17**(8), 4787–4792.
33 H. Liu, D. Fu, X. Li, J. Han, X. Chen, X. Wu, B. Sun, W. Tang, C. Ke, Y. Wu, Z. Wu and J. Kang, *ACS Nano*, 2021, **15**(5), 8244–8251.
34 A. M. Dibos, Y. Zhou, L. A. Jauregui, G. Scuri, D. S. Wild, A. A. High, T. Taniguchi, K. Watanabe, M. D. Lukin, P. Kim and H. Park, *Nano Lett.*, 2019, **19**(6), 3543–3547.
35 E. V. Calman, L. H. Fowler-Gerace, D. J. Choksy, L. V. Butov, D. E. Nikonov, I. A. Young, S. Hu, A. Mishchenko and A. K. Geim, *Nano Lett.*, 2020, **20**(3), 1869–1875.
36 Y. Huang, K. Yu, H. Li, K. Xu, Z. Liang, D. Walker, P. Ferreira, P. Fischer and D. E. Fan, *Adv. Mater.*, 2020, **32**, 2003439.

37 Z. Zheng, J. Chen, Y. Wang, X. Wang, X. Chen, P. Liu, J. Xu, W. Xie, H. Chen, S. Deng and N. Xu, *Adv. Mater.*, 2018, **30**, 1705318.
38 R. Zhang, D. Drysdale, V. Koutsos and R. Cheung, *Adv. Funct. Mater.*, 2017, **27**, 1702455.
39 X. Yu, N. Guijarro, M. Johnson and K. Sivula, *Nano Lett.*, 2018, **18**(1), 215–222.
40 H. Medina, J. G. Li, T. Y. Su, Y. W. Lan, S. H. Lee, C. W. Chen, Y. Z. Chen, A. Manikandan, S. H. Tsai, A. Navabi, X. Zhu, Y. C. Shih, W. S. Lin, J. H. Yang, S. R. Thomas, B. W. Wu, C. H. Shen, J. M. Shieh, H. N. Lin, A. Javey, K. L. Wang and Y. L. Chueh, *Chem. Mater.*, 2017, **29**, 1587.
41 B. Liu, Y. Ma, A. Zhang, L. Chen, A. N. Abbas, Y. Liu, C. Shen, H. Wan and C. Zhou, *ACS Nano*, 2016, **10**(5), 5153–5160.
42 C. Liu, G. Li, R. Di Pietro, J. Huang, Y.-Y. Noh, X. Liu and T. Minari, *Phys. Rev. Appl.*, 2017, **8**, 034020.
43 Z. Li, S. Yang, R. Dhall, E. Kosmowska, H. Shi, I. Chatzakis and S. B. Cronin, *ACS Nano*, 2016, **10**(7), 6836–6842.
44 T. D. Ngo, M. S. Choi, M. Lee, F. Ali, Y. Hassan, N. Ali, S. Liu, C. Lee, J. Hone and W. J. Yoo, *Adv. Sci.*, 2022, **9**, 2202465.
45 Y. Tian, C. Guo, S. Guo, T. Yu and Q. Liu, *Nano Res.*, 2014, **7**, 953–962.
46 Y. Tian, L. Jiang, X. Zhang, G. Zhang and Q. Zhu, *AIP Adv.*, 2018, **8**, 035105.
47 F. Xia, V. Perebeinos, Y. M. Lin, Y. Wu and P. Avouris, *Nat. Nanotechnol.*, 2011, **6**, 179–184.
48 S. Ross, P. Klement, A. M. Jones, N. J. Ghimire, J. Yan, D. G. Mandrus, T. Taniguchi, K. Watanabe, K. Kitamura, W. Yao, D. H. Cobden and X. Xu, *Nat. Nanotechnol.*, 2014, **9**, 268–272.
49 J. Guo, D. Xie, B. Yang and J. Jiang, *Solid-State Electron.*, 2018, **144**, 1.
50 M. Y. Li, C. H. Chen, Y. Shi and L. J. Li, *Mater. Today*, 2016, **19**, 322–335.
51 Z. Yang, L. Liao, F. Gong, F. Wang, Z. Wang, X. Liu, X. Xiao, W. Hu, J. He and X. Duan, *Nano Energy*, 2018, **49**, 103.
52 T. Shen, J. C. Ren, X. Liu, S. Li and W. Liu, *J. Am. Chem. Soc.*, 2019, **141**, 3110.
53 A. Li, Q. Chen, P. Wang, Y. Gan, T. Qi, P. Wang, F. Tang, J. Z. Wu, R. Chen, L. Zhang and Y. Gong, *Adv. Mater.*, 2019, **31**, 1805656.
54 N. N. Mude, R. N. Bukke and J. Jang, *Adv. Mater. Technol.*, 2022, 2101434.
55 Z. Cheng, *et al.*, *J. Mater. Chem. C*, 2022, **10**, 1511–1516.
56 N. R. Pradhan, J. Ludwig, Z. Lu, D. Rhodes, M. M. Bishop, K. Thirunavukkuarasu, S. A. McGill, D. Smirnov and L. Balicas, *ACS Appl. Mater. Interfaces*, 2015, **7**(22), 12080–12088.
57 H. Li, L. Ye and J. Xu, *ACS Photonics*, 2017, **4**, 823.
58 H. Im and S. Kim, *Adv. Electron. Mater.*, 2021, **7**, 2100003.
59 P. Lin, L. Zhu, D. Li, L. Xu, C. Pan and Z. Wang, *Adv. Funct. Mater.*, 2018, **28**, 1802849.